PAPER

Check for updates

Formation of cubic perovskite alloy containing the ammonium cation of 2D perovskite for high performance solar cells with improved stability†

Mi-Hee Jung *

The perovskite solar cells have demonstrated to be strong competitors for conventional silicon solar cells due to their remarkable power conversion efficiency. However, their structural instability is the biggest obstacle to commercialization. To address these issues, we prepared $(CH_3NH_3)_{1-x}(HC(NH_2)_2)_xPbI_3$ (CH_3NH_3 = MA, $HC(NH_2)_2$ = FA) perovskite alloys that contain ethylammonium (EA, $CH_3CH_2NH_3^+$) and benzylammonium (BA, $C_6H_5CH_2NH_3^+$) cations with no new additional two-dimensional (2D) perovskite phases. The crystal structures of alloy perovskites exhibit the cubic phase, which decreased the cation disorder and the intrinsic instability compared to 3D MAPbI$_3$ perovskite. The band gaps of the alloy perovskites are almost the same as the corresponding 3D perovskites, which exhibit a high refractive index, a large absorption coefficient, and paramagnetic properties for the production of high performance photovoltaic devices. After we constructed the solar cell with the configuration of regular (n–i–p) solar cells using the alloy perovskites, the power conversion efficiencies (PCE) of the $MA_{0.83}EA_{0.17}PbI_3$ perovskite solar cell showed the highest efficiency, which was 10.22%, under 1 sun illumination.

1. Introduction

The organic–inorganic hybrid halide perovskite (ABX$_3$, A = $CH_3NH_3^+$ (MA), $(NH_2)_2CH^+$ (FA), Cs^+, B = Pb^+, Sn^+, Ge^+ and X = Cl^-, Br^-, I^-) solar cells (PVSC) have achieved tremendous progress in recent years because their certified power conversion efficiencies (PCE) have increased from an initial 3.8% efficiency in 2009 to above 23% within a few years due to its excellent properties, which include a long electron diffusing length, a high optical absorption coefficient, and high ambipolar carrier transport. Despite this progress, their commercialization was mainly inhibited by the instability due to the humidity and oxygen in the ambient air. For example, the MAPbI$_3$ that was used first was easily decomposed due to humidity and oxygen. To challenge this issue, partially replacing the MAPbI$_3$ with FAPbI$_3$ increased the thermal stability, which better matched the solar spectrum. Compared with MAPbI$_3$, the FAPbI$_3$ has a low band gap of 1.47 eV,[1] which demonstrates higher thermal stability, mobility (4.4 cm^2 V^{-1} s^{-1}), and conductivity (1.1 × 10^{-7} (Ω cm)$^{-1}$).[2] However, FAPbI$_3$ suffers from the phase transition from the black perovskite phase, which is the cubic space group *Pm3m*, α-FAPbI$_3$, to the

yellow non-perovskite structure, which is the hexagonal space group *P6₃mc*, δ-FAPbI$_3$, at room temperature.[3–5] Moreover, the mixed perovskite $MA_{1-x}FA_xPbI_3$ exhibited poor light stability[6] and the 1D lead polyhalide framework[7] still remained in the crystal, which was also observed in the MAPbI$_3$, and this hindered the formation of a uniform film.

Herein, we address this problem with the incorporation of two-dimensional (2D) perovskites into the three-dimensional (3D) $MA_{1-x}FA_xPbI_3$ perovskites. The 2D layered structures can be subcategorized as (100), (110), and (111) oriented perovskites based on the different cuts from the 3D framework. The 2D perovskites have multiple quantum well structures by orderly combining the 2D inorganic framework with the organic constituents. Compared with the 3D perovskites, the 2D layered perovskites exhibit improved moisture stability, and they have much larger energy of formation and a higher degree of freedom, which result in the suppression of ion migration and enhanced device stability. However, even though the 2D layered perovskites improved the device stability, the relatively poor transportation of the photoelectron and the undesirable carrier loss inevitably occurred due to the lateral crystal orientation and the internal dielectric phase of the organic cations. It caused charge accumulation and radiative recombination losses at the interface of the device, and it should be solved in order to achieve a high efficiency solar cell. There are two main strategies that have been developed to enhance the device performance using 2D perovskites. One is increasing the number (n) of the inorganic layer, which involves some

Department of Nanotechnology and Advanced Materials Engineering, Sejong University, 209, Neungdong-ro, Gwangjin-gu, Seoul 05006, Republic of Korea. E-mail: mhjung@sejong.ac.kr; Fax: +82-2-3408-4342; Tel: +82-2-6935-2597

sacrifices for stability.[8] The other is the perpendicular crystal growth to the substrate to increase the effective charge transport. However, both of them still have limitations to approach the performance of 3D perovskites due to the narrower absorption in the range of the solar spectrum and the large exciton binding energy.[9,10] To avoid these issues, we incorporated ethylammonium (EA, $CH_3CHNH_3^+$) and benzylammonium (BA, $C_6H_5CH_2NH_3^+$) into the 3D $MA_{1-x}FA_xPbI_3$ perovskite within the range that did not form the 2D perovskite phase, which is the main distinction from the previous studies. The EA or BA incorporated $MA_{1-x}FA_xPbI_3$ perovskites show the cubic phase crystal system with contracted lattice and high cation disorder, which enables the systematic tuning of morphology, electronic properties, and improved stability of materials. The incorporation of 3–11 mol% of cations results in a stable alloy perovskite structure with no new phases formed. When the alloy cubic perovskites were applied into the regular (n–i–p) solar cell configuration (FTO/TiO₂ BL/TiO₂ MP/perovskite/Spiro-OMeTAD), the PCE of the $MA_{0.83}EA_{0.17}PbI_3$ perovskite shows the highest efficiency, which is 10.22%, under 1 sun illumination. This study gives the possibility of better controlling the perovskite solar cell structure with the neighboring layer and further improving the solar cell devices.

2. Experimental section

2.1. Starting materials

The lead oxide (PbO, 99%), hydriodic acid (HI, 57 wt% in H₂O), hypophosphorous acid (H₃PO₂, 50 wt% in H₂O), N,N-dimethylformamide (DMF, anhydrous, 99.8%), dimethyl sulfoxide (DMSO, anhydrous, ≥99.9%), methylamine hydrochloride (CH₃NH₃Cl, ≥98%), ethylamine hydrochloride (EACl, 98%), benzylamine hydrochloride (BACl), and chlorobenzene (CB, anhydrous, 99.8%) were purchased from Sigma–Aldrich, and they were used without further purification. The Spiro-MeOTAD and the phenyl-C₆₁-butyric acid methyl ester (PC₆₁BM, >99%) were purchased from Luminescence Technology Corporation. The poly(3,4-ethylenedioxythiophene)–poly(styrenesulfonate) (PEDOT:PSS, CLEVIOS Al4083) was purchased from Heraeus. The CH₃NH₃I (MAI) was synthesized by neutralizing equimolar amounts of a 57% w/w aqueous HI and a 40% w/w aqueous methylamine (CH₃NH₂). The white precipitate was collected by evaporating the solvent using rotary evaporation at 60 °C under reduced pressure.

2.2. Synthesis of $(MAPbI_3)_x(FAPbI_3)_y(EAPbI_3)_{1-x-y}$ perovskite alloy

A 100 mL two-necked round-bottom flask was charged with 5.0 mL of stabilized hydriodic acid (HI, 57 wt% in H₂O) with a trace amount of hypophosphorous acid (1.5% H₃PO₂). The mixture was degassed with nitrogen for 1 min, and the flask was kept under nitrogen for the duration of the experiment. The flask was heated in an oil bath to 120 °C, and the PbO, which weighed 0.4464 g and contained 2 mmol, was added. It was then stirred vigorously until the solid had completely dissolved. The MACl, which weighed 0.1756 g and contained 2.6 mmol, and formamidine acetate, which weighed 0.1756 grams and

contained 2.6 mmol, powders were then added to the flask, which immediately resulted in a black precipitate. We added a small amount of HI solution into the previous solution to completely re-dissolve the black powder by vigorously stirring the mixture. When the solution became a bright yellow, the EACl powder, which weighed 0.0163 g and contained 0.2 mmol, was subsequently added directly above the solution. The stirring was then discontinued, and the solution was left to cool to room temperature. As soon as the supersaturated yellow solution was removed from the hot plate and left to cool to the ambient temperature, black precipitates were generated. The precipitate was filtered and measured for the crystal structure, optical properties, and solar cell fabrication.

2.3. Synthesis of the $(MAPbI_3)_x(FAPbI_3)_y((BA)_2PbI_4)_{1-x-y}$ perovskite alloy

A 100 mL two-necked round-bottom flask was charged with 5.0 mL of stabilized hydriodic acid (HI, 57 wt% in H₂O) with a trace amount of hypophosphorous acid (1.5% H₃PO₂). The mixture was degassed with nitrogen for 1 min, and the flask was kept under nitrogen for the duration of the experiment. The flask was heated in an oil bath to 120 °C, and the PbO, which weighed 0.4464 g and contained 2 mmol, was added, and the mixture was then stirred vigorously until the solid had completely dissolved. The MACl, which weighed 0.1756 g and contained 2.6 mmol, and formamidine acetate, which weighed 0.1249 g and contained 1.2 mmol, powders were then added to the flask, which immediately resulted in a black precipitate. We added a small amount of the HI solution into the previous solution to completely dissolve the black powder by stirring the mixture vigorously. When the solution became a bright yellow, the BACl powder, which weighed 0.0287 g and contained 0.2 mmol, was subsequently added directly above the solution. The stirring was then discontinued, and the solution was left to cool to room temperature. As soon as the supersaturated yellow solution was removed from the hot plate and left to cool to an ambient temperature, a black precipitate was generated. The precipitate was filtered and measured for the crystal structure, optical properties, and solar cell fabrication.

2.4. Growth of the perovskite single-crystal alloy

The mixed $MA_{0.67}FA_{0.33}PbI_3$, $MA_{0.65}FA_{0.3}EA_{0.05}PbI_3$, and $MA_{0.65}FA_{0.3}BA_{0.05}PbI_3$ single crystals were prepared using inverse temperature crystallization (ITC).[11–14] In brief, for the $MA_{0.67}FA_{0.33}PbI_3$ single crystal growth, a 1.0 M MAPbI₃/FAPbI₃ perovskite precursor solution was prepared by dissolving equimolar PbI₂ and MAI/FAI in γ-butyrolactone at 60 °C overnight. The solution was filtered using a PTFE membrane with a 0.2 μm pore size. The seed crystals that were 1–2 mm in size were first prepared by placing a 2 mL precursor solution at 110 °C for 3 h in an oil bath under ambient conditions. For the large crystal growth, only one seed was used. The seed crystal was placed into the fresh precursor solution, which was heated at 110 °C for 3 h to obtain the crystal growth. To further increase the crystal size, the temperature was set to 120 °C for another hour. By repeating the above process multiple times, larger and larger perovskites

will be obtained. The $MA_{0.65}FA_{0.3}EA_{0.05}PbI_3$ and the $MA_{0.65}$-$FA_{0.3}BA_{0.05}PbI_3$ single crystals also were prepared using the above method except for the 1.0 M $MAPbI_3$/$FAPbI_3$/$EAPbI_3$ and $MAPbI_3$/$FAPbI_3$/$(BA)_2PbI_4$ concentrations, which were used according to the respective stoichiometric coefficients.

2.5. Single crystal X-ray crystallographic analysis

A crystal of the perovskites was coated with paratone-*N* oil, and the diffraction data were measured at 100 K, 298 K, and 450 K with synchrotron radiation ($\lambda = 0.61000$ Å) on an ADSC Quantum-210 detector at BL2D SMC with silicon (111) double crystal monochromator (DCM) at the Pohang Accelerator Laboratory (PAL), Korea. The PAL BL2D-SMDC program[15] was used for data collection (detector distance is 63 mm, omega scan; $\Delta\omega = 3°$, exposure time is 1 s per frame), and HKL3000sm (Ver. 703r)[16] was used for cell refinement, reduction, and absorption correction. The crystal structure of the perovskite was solved by the direct method with the SHELXT-2014 program[17] and refined by full-matrix least-squares calculations with the SHELXL-2014 program package.[18]

2.6. Characterizations

The steady-state PL spectra were measured by dividing and guiding the PL signal through an optical fiber using a HORIBA LabRAM HR Evolution confocal RAMAN microscope. A 532 nm laser (0.01% power) was used to excite all the samples at 50× magnification. The time-resolved PL (TRPL) study was performed using an inverted-type scanning confocal microscope (MicroTime-200, PicoQuant, Germany) with a 60× (air) objective. The lifetime measurements were performed at the Korea Basic Science Institute (KBSI), Daegu Center, Korea. The single-mode pulsed diode lasers, which used 375 nm and 470 nm with a pulse width of ∼30 ps, were used as the excitation sources. A dichroic mirror (Z375RDC and AHF), a long pass filter (HQ405lp and AHF), a 75 μm pinhole, a band-pass filter, and an avalanche photodiode detector (PDM series and MPD) were used to collect the emissions from the samples when the 375 nm laser irradiated. A dichroic mirror (490 DCXR and AHF), a long-pass filter (HQ500lp, AHF), a 75 μm pinhole, and a single photon avalanche diode (PDM series and MPD) were used to collect emissions when 470 nm laser irradiated. Time-correlated
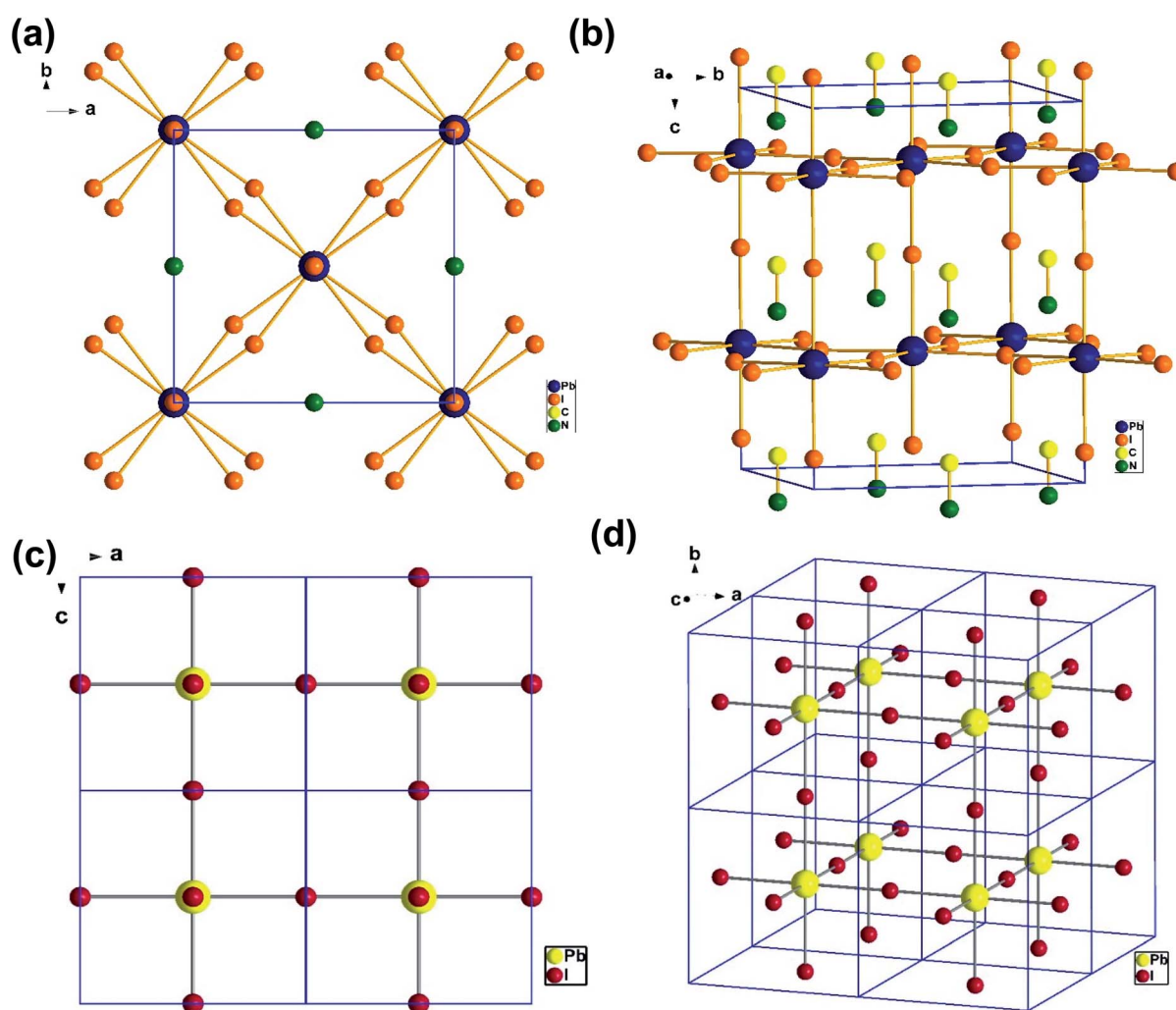

Fig. 1 The crystal structure of $MAPbI_3$ from the (a) top-down view along the *b* axis and (b) side view of the tetragonal unit cell. The crystal structure of $MA_{0.5}EA_{0.5}PbI_3$ from the (c) a top-down view along the *b* axis and (d) a view of the cubic unit cell.

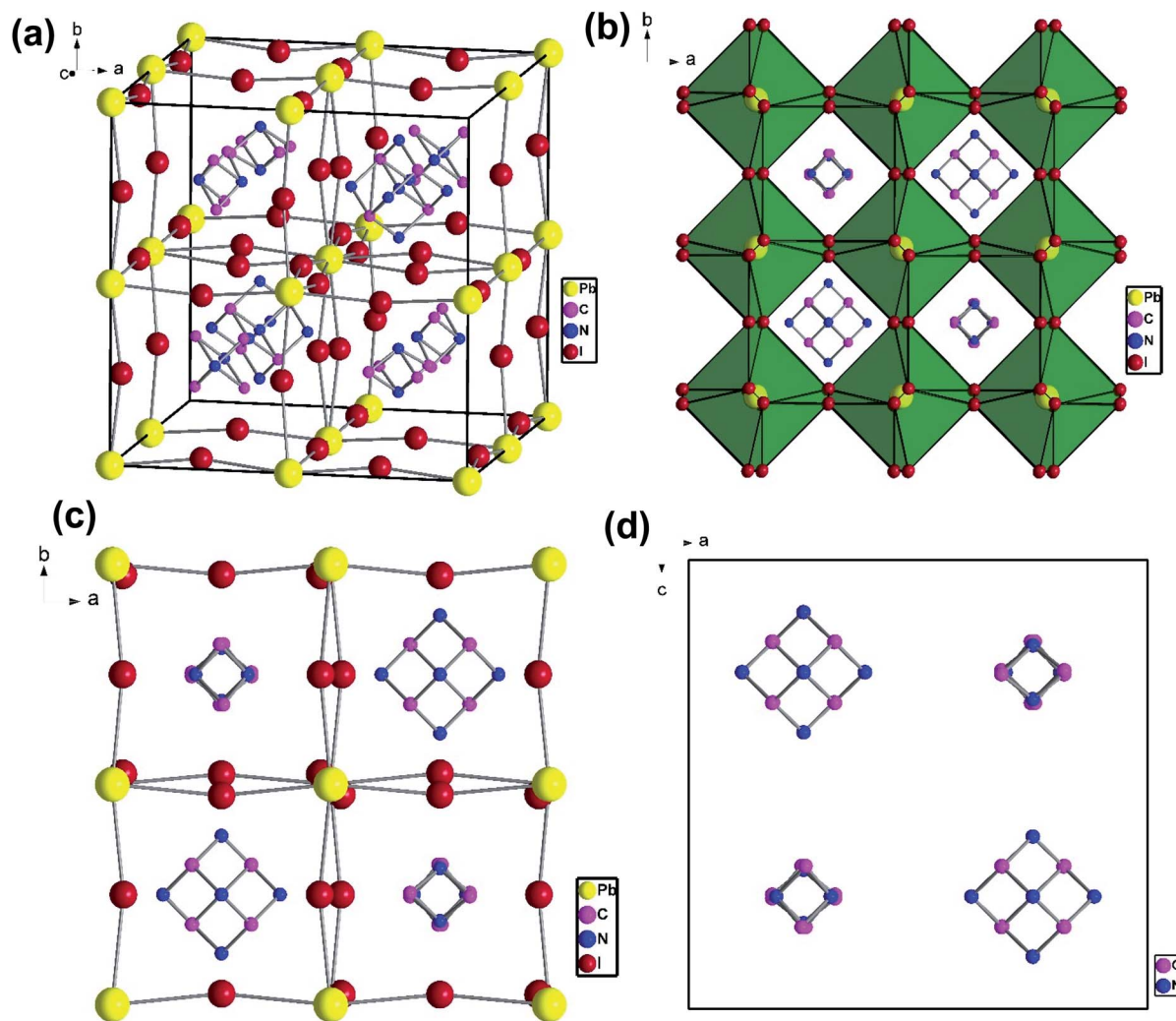**Fig. 2** The crystal structure of $MA_{0.65}FA_{0.3}EA_{0.05}PbI_3$ to show the cation disorder of MA^+ and FA^+ from (a) a side view of the cubic unit cell and (b–d) a top view along the c axis.

single-photon counting (TCSPC) technique was used to count fluorescence photons. The TRPL images consisted of 200×200 pixels, which were recorded using the time-tagged time-resolved (TTTR) data acquisition method. The exponential fittings for the obtained PL decay with a temporal resolution of 16 ps were performed using SymPhoTime-64 software (Ver. 2.2) with the exponential decay model $I(t) = \sum A_i e^{-t/\tau_i}$, where $I(t)$ is the time-dependent PL intensity, A is the amplitude, and τ is the PL lifetime. The ultraviolet photoelectron spectroscopy (UPS) measurements were conducted using an AXIS ultra-delay line detector (DLD) (Kratos Inc.) in KBSI, Daejeon. The He I (21.22 eV) emission line was employed as a UV source. The optical diffuse reflectance spectra were measured using the Agilent (Cary-5000) UV-vis-NIR system. Polytetrafluoroethylene was used as the non-absorbing reference material with 100% reflectance. The reflectance *versus* the wavelength was converted to the absorption data to calculate the band gap (E_g) using the Kubelka–Munk equation,[19,20] $\alpha/S = (1 - R)^2(2R)^{-1}$, where R is the reflectance and α and S are the absorption and scattering coefficients. The X-ray diffraction (XRD) patterns were

measured using an Empyrean PANalytical instrument with a Cu Kα radiation (40 kV, 30 mA, and $\lambda = 1.54056$ Å) and a Ni filter with a graphite monochromator. The morphology of the perovskite film was obtained using field emission scanning electron microscopy (FE-SEM, Hitachi SU8010). The magnetic properties were analysed in the powder samples by the magnetization curves [M − H] using a physical property measurement system, a Quantum Design PPMS 6000, that was equipped with a vibrating sample magnetometer, which was a VSM Micro Sense EV9. The M − H was measured by varying the applied field from 30 kOe to −30 kOe and then back to 30 kOe to characterize a full hysteresis loop at room temperature. The measurements of optical-pump THz probe spectroscopy were conducted at the PAL. The construction of the THz generation was well explained in the previous report.[21] The wavelength of the pump beam is 400 nm with an intensity of 40 μJ cm^{-2}. We measure the THz time domain signal in the spectral range from 0.2 up to 2.5 THz. The transmitted THz frequency domain spectra were acquired by the fast Fourier transforms (FFT) to each time domain THz pulse waveform.
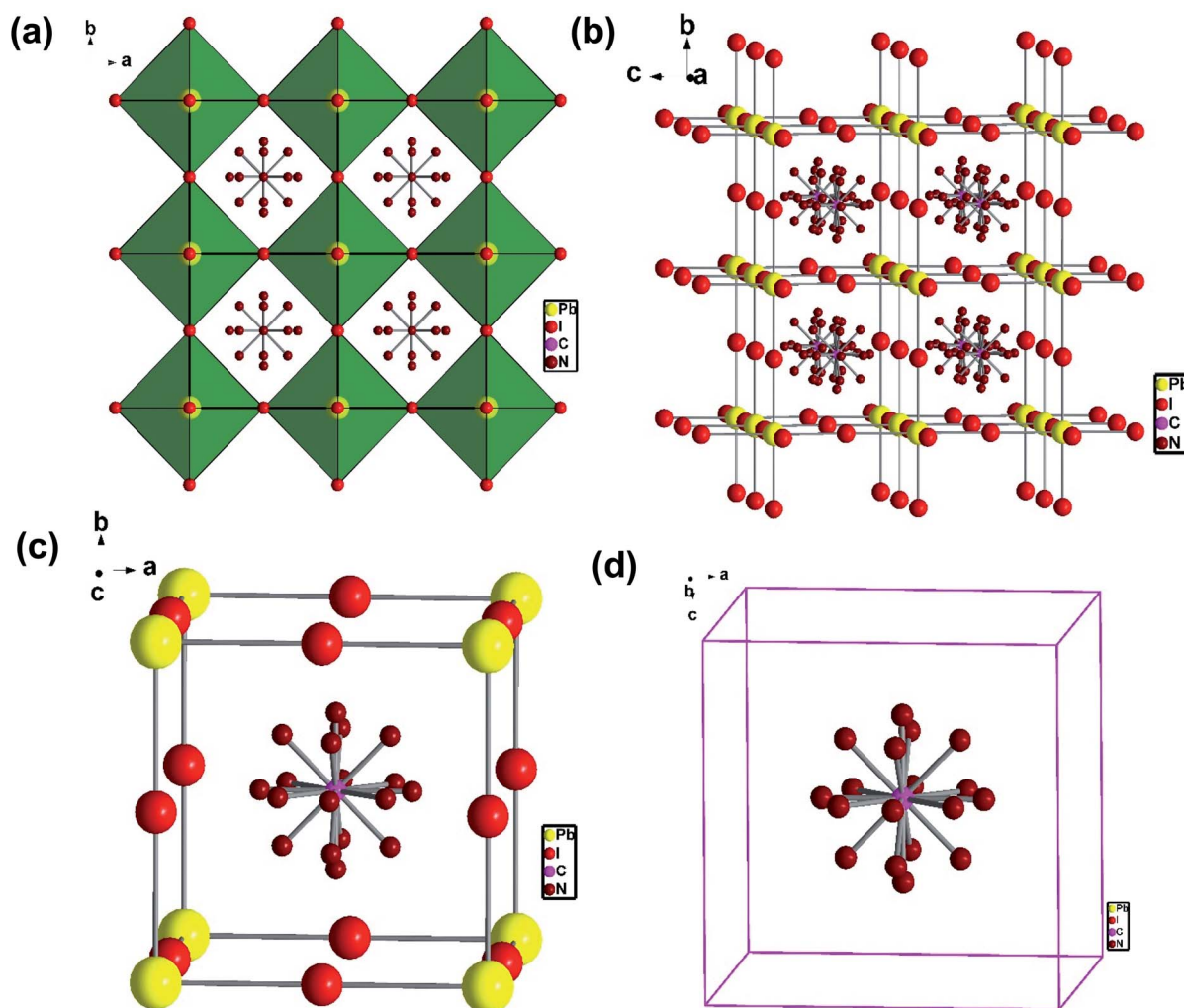
Fig. 3   (a) The crystal structure of the $MA_{0.65}FA_{0.3}BA_{0.05}PbI_3$ perovskite, (b) the side view of the disordering of FA^+, and (c, d) the disordering FA^+ cation in a cubic unit cell.

Hall effect measurements were conducted in air using four contacts The Hall bar method utilized DC current flowing through perovskite pellet applied using a Keithley Model 2400, and the Hall voltage was recorded using a Keithley Model 4200. A field strength of 0.533T was applied.

2.7.   Solar cell fabrication

The N-type TiO_2 layer formation used the following method. A 50 nm compact layer of TiO_2 was deposited on the FTO substrate by spin coating at 2000 rpm for 30 s and using a mildly acidic solution of titanium isopropoxide (TTIP) in ethanol that contained a 350 μL TTIP in 5 mL EtOH with 0.013 M HCl. The sintering process was then conducted at 550 °C for 30 min. A mesoporous (MP) TiO_2 layer was spin-coated on the TiO_2 compact layer with a diluted TiO_2 paste, which was DYESOL-30NRD, with ethanol with a ratio of 1 : 3.5 w/w at 500 rpm for 5 s, 3000 rpm for 10 s, and 6000 rpm for 30 s. The substrate was further treated with a 20 mM $TiCl_4$ aqueous solution at 70 °C for 30 min, rinsed with deionized water and ethanol, and then sintered at 500 °C for 30 min. The 1.25 M prepared $(MAPbI_3)_x(FAPbI_3)_y(EAPbI_3)_{1-x-y}$ and the

$(MAPbI_3)_x(FAPbI_3)_y((BA)_2PbI_4)_{1-x-y}$ perovskites according to the stoichiometric coefficient were dissolved in DMF and DMSO solvents, which was 4 : 1 vol%. The solution was spin coated on the N-type TiO_2 layer at 4000 rpm for 30 s, which was followed by the annealing process at 100 °C for 30 min. A solution for the Spiro-MeOTAD coating was prepared by dissolving a 72.3 mg Spiro-MeOTAD in 1 mL of chlorobenzene, in which 28.8 μL of 4-*tert*-butyl pyridine and a 17.5 μL of lithium bis(tri-fluoromethanesulfonyl)imide solution (520 mg Li-TSFI in 1 mL acetonitrile (Sigma–Aldrich, 99.8%) were added.[22] The Spiro-MeOTAD was deposited at 4000 rpm for 30 s on the perovskite layer. The gold layer of 800 Å for the counter electrode was deposited on the perovskite layer with thermal evaporation at 1.5 Å s^{-1}. The photocurrent (J_{sc}) and the photovoltage (V_{oc}) of solar cells were measured with an active area of 0.175 cm^2 using Keithley 2400 source meter and a Newport solar simulator (model 91192), which offered simulated solar light at AM 1.5 (100 mW cm^{-2}), which was calibrated with a NIST-certified monocrystalline Si solar cell (Newport 532 ISO1599). The incident photon to the current efficiency (IPCE) was measured using an IQE200B designed by the Newport Corporation. A 100 W Xenon lamp was applied as the
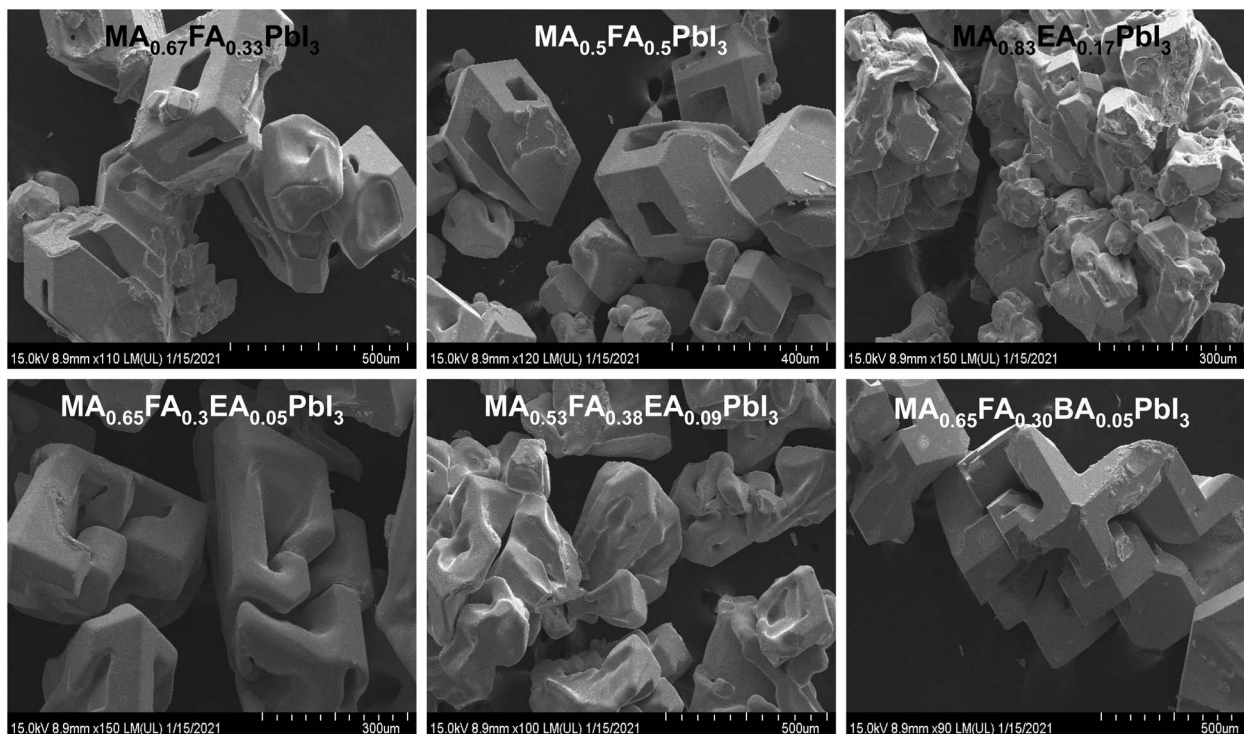
Fig. 4 The SEM images of single crystal of $MA_{0.67}FA_{0.33}PbI_3$, $MA_{0.5}FA_{0.5}PbI_3$, $MA_{0.83}EA_{0.17}PbI_3$, $MA_{0.65}FA_{0.3}EA_{0.05}PbI_3$, $MA_{0.53}FA_{0.38}EA_{0.09}PbI_3$, and $MA_{0.65}FA_{0.30}BA_{0.05}PbI_3$ perovskites.

light source for the monochromatic beam. A reference silicon photodiode (NIST-calibrated photodiode G425) was used for the calibration of the monochromatic light intensity.

3. Results and discussion

To understand the alloy phase of the $MA_{0.5}EA_{0.5}PbI_3$ perovskite, a single crystal XRD measurement was performed to study the
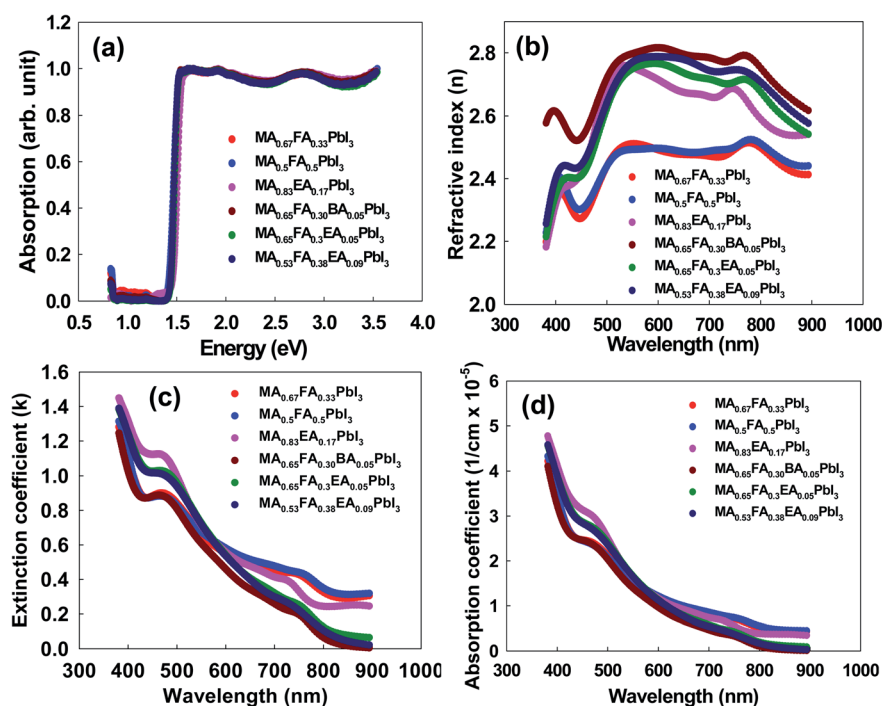

Fig. 5 (a) The UV-visible diffuse reflectance spectra, (b) the real, n, refractive index, (c) the imaginary, k, refractive index, and (d) the adsorption coefficient for 3D $MAPbI_3$ and alloy perovskites.
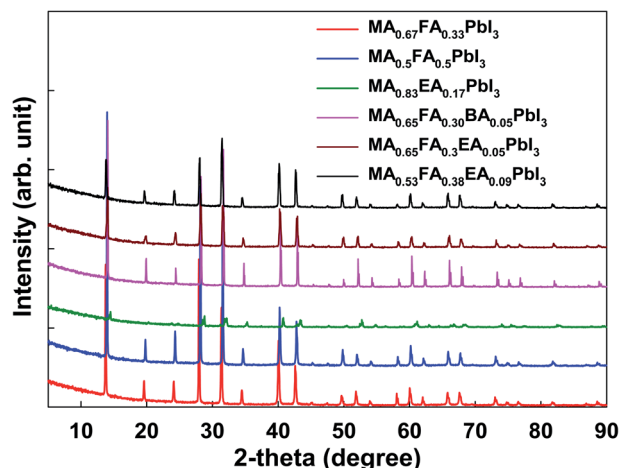
Fig. 6 The powder X-ray diffraction of 3D MAPbI$_3$ and the alloy perovskites.

crystal structure, which could explain the mechanism of the inhibition of the phase transition with the alloy formation. As shown in Fig. 1c and d, the unit cell of MA$_{0.5}$EA$_{0.5}$PbI$_3$ shows a cubic $Pm\bar{3}m$ space group with $a = b = c = 6.3257(7)$ Å and a cell volume of 253.12(8) Å^3. By comparing the unit cell parameters of MA$_{0.5}$EA$_{0.5}$PbI$_3$ with those of the MAPbI$_3$ and the EAPbI$_3$, the unit cell volume of MA$_{0.5}$EA$_{0.5}$PbI$_3$ was contracted from 990.3(3) Å^3 and 1080.1(4) Å^3 for the MAPbI$_3$ (tetragonal and $I4cm$) and the EAPbI$_3$ (orthorhombic and $Pnma$), which are illustrated in Fig. 1c and d, to 253.12(8) Å^3. The lattice contraction of MA$_{0.5}$-EA$_{0.5}$PbI$_3$ can be probably attributed to the fact that with the introduction of two different cations, which are MA and EA, the disordering of cations was fully developed due to the change in the hydrogen bonding between the organic cation hydrogen atom and the iodide ion of the inorganic lattice. This is the hydrogen bonding disruption with a dissimilar hydrogen bonding strength, and the orientation and the acidity are illustrated by the FA$_x$MA$_{1-x}$PbI$_3$ crystal structure,[23] which reduces the octahedral volume of the A site cation that is surrounded by the PbI$_6$ octahedra in the unit cell. This occurrence is mentioned by Xie *et al.*[13] Therefore, the Goldschmidt tolerance factor (α)[24] for this perovskite structure approaches 1, which is mostly found in the cubic perovskite. We introduced a ternary organic cation based perovskite to understand the cubic phase stabilization, which is essential for device stability. As shown in Fig. 2, the crystal structure of MA$_{0.65}$FA$_{0.3}$EA$_{0.05}$PbI$_3$ shows the cation disorder of MA$^+$ and FA$^+$ in the crystal. As a small amount of the EA$^+$ cation was incorporated into the FA$_x$MA$_{1-x}$PbI$_3$ crystal structure, the MA$^+$ disorder in the unit cell was over 16 possible sites, but the FA$^+$ disorder in the crystal was over 8 possible sites, which are illustrated in Fig. 2a–d. The MA$_{0.65}$FA$_{0.3}$BA$_{0.05}$PbI$_3$ perovskite shows the FA$^+$ disorders in the crystal over 9 possible sites, which is illustrated in Fig. 3a–d. These results suggest that the incorporation of the cation plays an important role in cubic phase stabilization because it has a stronger dipole and more flexible orientation, which results in a high degree of cation disorder.[13] According to the

Goldschmidt tolerance factor, t, is defined as follows: $t = (r_A + r_x)/\sqrt{2}(r_B + r_x)$, where r_A and r_B are the ionic radius of the A and B site cations, respectively, and r_x is the ionic radius of the anion.[24,25] The perovskite structure can be predicted using a simple geometric consideration; for a 3D perovskite, the value of $0.8 \leq t \leq 1$. A tolerance factor of $t \approx 1$ results in the formation of a cubic perovskite structure, whereas lower t values result in a cubic structure of lower symmetry, such as tetragonal or orthorhombic. Herein, we calculated the tolerance factor for our compounds. The resultant values including the parameters are shown in Table S1 in the ESI.† The tolerance factors of MA$_{0.67}$FA$_{0.33}$PbI$_3$, MA$_{0.5}$FA$_{0.5}$PbI$_3$, MA$_{0.83}$EA$_{0.17}$PbI$_3$, MA$_{0.65}$-FA$_{0.3}$EA$_{0.05}$PbI$_3$, MA$_{0.53}$FA$_{0.38}$EA$_{0.09}$PbI$_3$, and MA$_{0.65}$FA$_{0.30}$BA$_{0.05}$-PbI$_3$ perovskites are 0.9363, 0.9491, 0.9317, 0.9400, 0.9508, and 0.9653, respectively. The tolerance factors of all compounds indicate the 3D perovskite structure, consistent with the cubic phase in single crystal XRD measurement.

Fig. 4 shows the SEM images of alloy perovskite crystals with an irregular shape, indicating the formation of the alloy crystal rather than a perfect crystal phase. Especially, MA$_{0.83}$EA$_{0.17}$PbI$_3$ shows an aggregated shape of the crystal phase. As a result, MA$_{0.83}$EA$_{0.17}$PbI$_3$ thin film exhibits a very compact film, as shown in Fig. 10. The morphology of 2D perovskite films generally shows plate-like morphology because it reflects the crystal shape and orientation with 2D characteristics. In contrast, 3D perovskite film exhibits larger grain size and denser stacking in the perpendicular direction to the substrate in comparison with the 2D perovskite. This is attributed to the crystal orientation of the 3D perovskite phase. For example, Lian *et al.*[26] found that larger colloidal size plays an important role in the formation of high quality film and large grains. Lv *et al.*[27] showed that the film quality is affected by particle sizes of the aggregate of the precursor. Therefore, we speculate that the aggregate shape of the MA$_{0.83}$EA$_{0.17}$PbI$_3$ crystal could induce the formation of high quality films.

To assess the optical characteristics, we measured the absorption spectra, the optical constants (n and k), and the absorption coefficient for the perovskites. The absorption spectra, which are illustrated in Fig. 5a, are similar for all the perovskites. The band gap energies were determined to be 1.41 eV, 1.40 eV, 1.46 eV, 1.42 eV, 1.43 eV, and 1.42 eV for MA$_{0.67}$FA$_{0.33}$PbI$_3$, MA$_{0.5}$FA$_{0.5}$PbI$_3$, MA$_{0.83}$EA$_{0.17}$PbI$_3$, MA$_{0.65}$-FA$_{0.3}$EA$_{0.05}$PbI$_3$, MA$_{0.53}$FA$_{0.38}$EA$_{0.09}$PbI$_3$, and MA$_{0.65}$FA$_{0.30}$BA$_{0.05}$-PbI$_3$ perovskites, respectively. This result indicates that the band gaps show only negligible difference because incorporated cations do not form the 2D perovskites, showing the same features as the 3D perovskite structure. The approach is attractive due to its suitable band gap for its derived perovskite solar cells and also can be applied to improve the phase stability successfully, as shown in Fig. 12b. This indicates that the optical properties were mainly governed by the inorganic perovskite part of the structure. The main difference comes from the distortion of the structure, which is represented by the Pb–I–Pb equatorial tilting angles. Herein, all the perovskites have cubic crystal structures, having the value of 180° in the Pb–I–Pb framework. This result reflected that insulating the organic
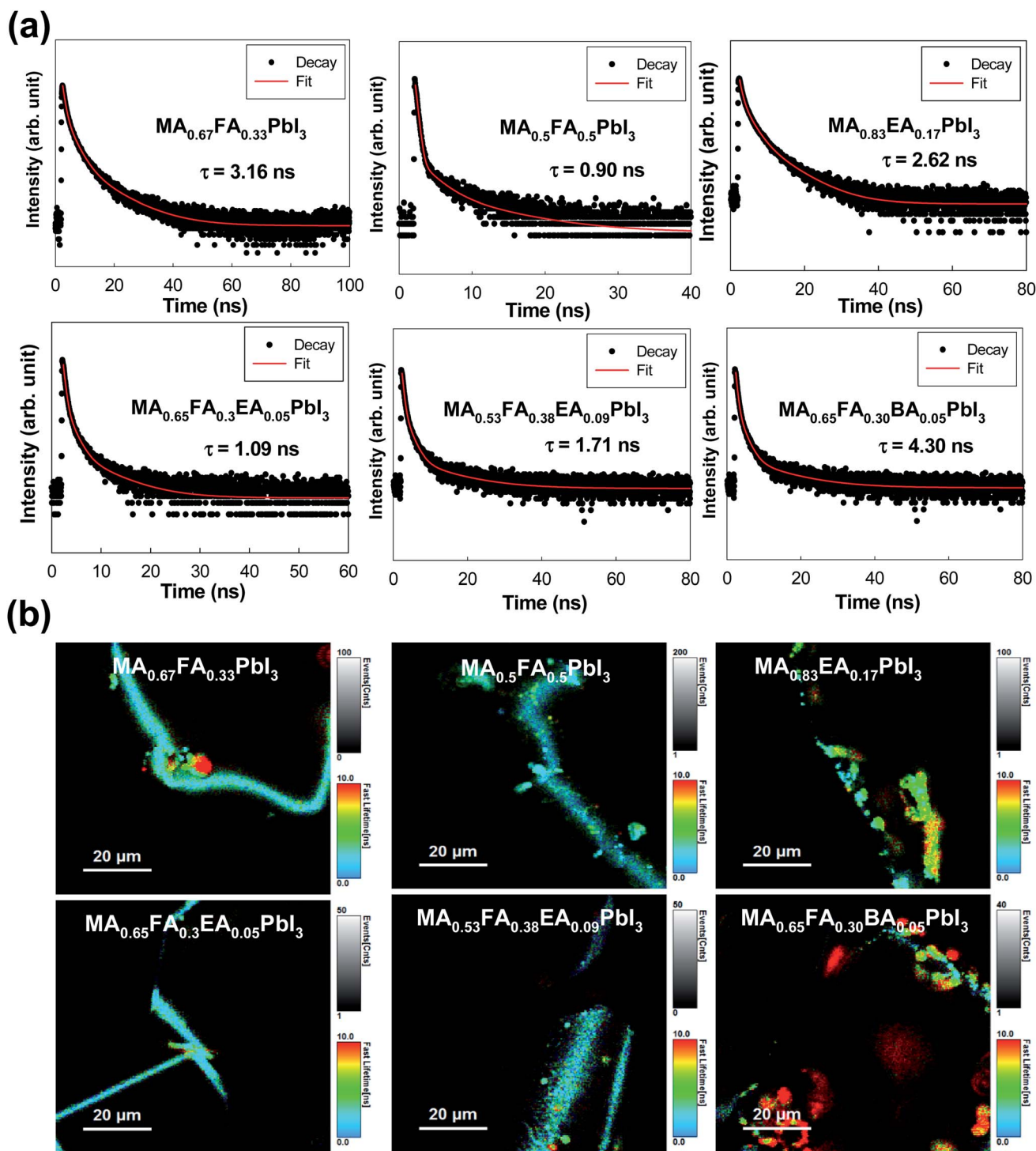
(a)

(b)

Fig. 7 (a) The transient photoluminescence decay profile of single crystal $MA_{0.67}FA_{0.33}PbI_3$, $MA_{0.5}FA_{0.5}PbI_3$, $MA_{0.83}EA_{0.17}PbI_3$, $MA_{0.65}FA_{0.3}EA_{0.05}PbI_3$, $MA_{0.53}FA_{0.38}EA_{0.09}PbI_3$, and $MA_{0.65}FA_{0.30}BA_{0.05}PbI_3$ perovskites at room temperature. The fitting results, which are the solid curves, were also included for comparison. (b) The image mapping of the emission decay of the $MA_{0.67}FA_{0.33}PbI_3$, $MA_{0.5}FA_{0.5}PbI_3$, $MA_{0.83}EA_{0.17}PbI_3$, $MA_{0.65}FA_{0.3}EA_{0.05}PbI_3$, $MA_{0.53}FA_{0.38}EA_{0.09}PbI_3$, and $MA_{0.65}FA_{0.30}BA_{0.05}PbI_3$ perovskite single crystals.

layer has a negligible effect on the optical properties of mixed perovskite structures.[28,29] The optical constants of perovskites, which are shown in Fig. 5b and c, were fitted based on the Gaussian oscillator, which used preferences to determine the band gap for the transparent organics, and the semiconductor

materials because they allow a shorter absorption tail. The value of the refractive index (n) for each material had a shoulder at 440 nm with the lowest value, and it showed an approximately constant value from 500 nm to 800 nm in the entire visible region and then decreased in the IR region. Compared to

Table 1 Photoluminescence lifetime results of 3D alloy perovskites from the transient photoluminescence[a]

Perovskites	A_1/%	τ_1/ns	A_2/%	τ_2/ns	A_3/%	τ_3/ns	τ/ns	τ_{amp}/ns
$MAPbI_3$	41.67	0.43	48.33	1.82	10.00	3.83	2.18	1.43
$MA_{0.67}FA_{0.33}PbI_3$	74.52	0.77	23.16	2.74	2.31	10.00	3.16	1.44
$MA_{0.5}FA_{0.5}PbI_3$	98.68	0.25	1.14	2.00	0.18	9.10	0.90	0.29
$MA_{0.83}EA_{0.17}PbI_3$	65.79	0.63	30.15	2.13	4.06	6.80	2.62	1.33
$MA_{0.65}FA_{0.3}EA_{0.05}PbI_3$	89.65	0.34	9.82	1.31	0.52	6.80	1.09	0.47
$MA_{0.53}FA_{0.38}EA_{0.09}PbI_3$	86.82	0.40	12.58	1.56	0.60	9.90	1.71	0.60
$MA_{0.65}FA_{0.30}BA_{0.05}PbI_3$	85.75	0.32	12.64	2.10	1.61	13.00	4.30	0.74

[a] The emission decay was analyzed using the equation: $I(t) = A_1 \exp(-t/\tau_1) + A_2 \exp(-t/\tau_2) + A_3 \exp(-t/\tau_3) + \ldots$, where $\sum_i A_i/(A_1 + A_2 + A_3 + \ldots) = 1$, the average lifetime, $\langle\tau\rangle$, is defined by $\tau = \sum_i A_i\tau_i^2 / \sum_i A_i\tau_i$, and τ_{amp} is the amplitude of average lifetime.

$FA_xMA_{1-x}PbI_3$ perovskites, the 2D perovskites that incorporated the 3D $MA_{1-x}FA_xPbI_3$ perovskites showed higher n values. The value of the extinction coefficient (κ) of perovskites, which is the imaginary part of the refractive index, substantially decreases as a function of the wavelength. The absorption coefficients of all the perovskites showed a strong absorption above the band edge, which indicates direct band gap materials. This is illustrated in Fig. 5d.

As shown in Fig. 6, except for $MA_{0.5}EA_{0.17}PbI_3$ perovskite, the powder XRD patterns of all the perovskites are similar to those of α-$FAPbI_3$ with slightly enlarged diffraction angles caused by the MA^+, BA^+, and EA^+ incorporation, which indicates the same cubic crystal phase as that of α-$FAPbI_3$. In the previous reports,[13,14] α-$FAPbI_3$ was easily converted from a pristine α-phase to a non-perovskite β-phase due to its thermodynamically unstable structure. However, the cation incorporated α-$FAPbI_3$ phase exhibits superior stability in ambient air as well as thermal stability that results from a thermodynamically stable structure and high crystallinity. We present the powder XRD patterns and simulated patterns from single crystal XRD for $MA_{0.83}EA_{0.17}PbI_3$, $MA_{0.65}FA_{0.30}BA_{0.05}PbI_3$, and $MA_{0.65}FA_{0.3}$-$EA_{0.05}PbI_3$ perovskites in Fig. S1 in the ESI.† The powder XRD patterns have almost the same features as the simulated patterns from the single crystal XRD. As shown in Fig. 6, except for $MA_{0.83}EA_{0.17}PbI_3$, the perovskites, the powder XRD patterns of all the perovskites are similar to those of α-$FAPbI_3$ because it show cubic crystal structures. However, $MA_{0.83}EA_{0.17}PbI_3$ without FA has poor crystallinity and shows a different crystal structure compared to other perovskites. The $MA_{0.83}EA_{0.17}PbI_3$ compound is an alloy of 3D $MAPbI_3$ and 1D $EAPbI_3$ ($EAPbI_3$ is crystallized to a long chain-like 1D structure, which consists of only face-sharing PbI_6), not the 2D layered structures (($EA)_2(MA)_{n-1}Pb_nI_{3n+1}$). Thus, since the XRD pattern of $MA_{0.83}EA_{0.17}PbI_3$ reflects the property of the alloy compound, 1D $EAPbI_3$, and 3D $MAPbI_3$ perovskite structures, we speculate that the intensity of the diffraction is weak compared to other alloy perovskites.

As shown in Fig. 7, we measured the TRPL in order to study the kinetics of the excitons and the free carriers in the mixed perovskites. The TRPL profiles were fitted with three exponential decays, and the detailed fitting parameters are listed in Table 1. The decay component, τ_1, is assigned to the non-

radiative recombination by the trap states of the perovskite crystal structure, and the decay processes (τ_2 and τ_3) corresponded to the radiative recombination from the bulk perovskite.[30,31] As shown in Table 1, the $MAPbI_3$ exhibits 0.43 ns (41.67%), 1.82 ns (48.33%), and 3.83 ns (10.00%) for τ_1, τ_2, and τ_3, respectively. Except for the $MA_{0.67}FA_{0.33}PbI_3$ and the $MA_{0.83}EA_{0.17}PbI_3$ perovskites, the PL lifetimes of all the
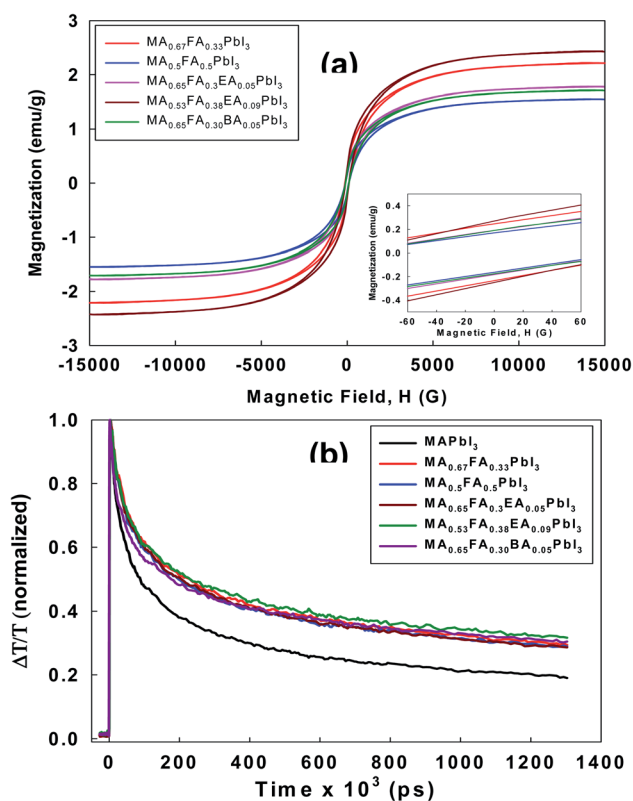

Fig. 8 (a) The magnetic hysteresis curves of the $MA_{0.67}FA_{0.33}PbI_3$, $MA_{0.5}FA_{0.5}PbI_3$, $MA_{0.65}FA_{0.3}EA_{0.05}PbI_3$, $MA_{0.53}FA_{0.38}EA_{0.09}PbI_3$, and $MA_{0.65}FA_{0.30}BA_{0.05}PbI_3$ perovskites measured using VSM at room temperature. The inset is the low-field portion that shows the HC values. (b) Charge carrier dynamics measured with optical pump-THz probe spectroscopy. The wavelength of the pump beam is 400 nm with the intensity of 40 μJ cm^{-2}. The THz time domain signals were collected in the spectral range from 0.2 to 2.5 THz.

perovskites were predominantly determined by the τ_1 component, because the values of A_1 are in the range of 85.75% to 98.68%, and the $MA_{0.67}FA_{0.33}PbI_3$ and the $MA_{0.83}EA_{0.17}PbI_3$ perovskites represent an A_2 that is 23.16% for $\tau_2 = 2.74$ and A_2 of 30.15% for $\tau_2 = 2.13$, respectively. In this respect, these perovskites showed much more efficient exciton recombination, which results in a decrease in the generation of free carriers compared to other perovskites. As a consequence, all of these situations have shown that the PL lifetimes of the alloyed perovskites do not improve significantly compared to the 3D perovskite, $MAPbI_3$. It was observed that there were decreases in the $MA_{0.5}FA_{0.5}PbI_3$, the $MA_{0.65}FA_{0.3}EA_{0.05}PbI_3$, and the $MA_{0.53}FA_{0.38}EA_{0.09}PbI_3$ perovskites, which are illustrated in Fig. 7a. Except for the $MA_{0.65}FA_{0.30}BA_{0.05}PbI_3$, the image mapping of PL lifetimes, which is illustrated in Fig. 7b, indicates that the alloyed perovskites have a short carrier lifetime compared to that of $MAPbI_3$.

All the perovskites in this study showed a cubic crystal structure, which is a very highly symmetric crystal system. However, previous reports[32] found that twining was observed in $MAPbI_3$ as an intrinsic functionality regardless of changes in the composition. This is often commonly observed in the transformation from the high symmetry phase to the low symmetry phase, which is also called the cubic phase to the tetragonal phase. These features have a significant impact on optical properties. In particular, the perovskite layer is composed of a tiny crystalline domain, and natural disordering is the driving force to produce the relatively long-lived spin-1/2 electron–hole pairs.[33] Thus, the generation and the recombination of the exciton may be influenced by a magnetic field. In consideration of this, we performed the measurement of magnetic properties for the alloy perovskites using VSM. As shown in Fig. 8a, all the perovskites showed a clear paramagnetic response. This paramagnetism is related to the unique crystal orientation of alloy perovskites. According to the related hysteresis loops in Fig. 8a, the coercivity (H_{ci}) is 114.57 Oe, 98.546 Oe, 102.10 Oe, 101.06 Oe, and 101.13 Oe for $MA_{0.67}FA_{0.33}PbI_3$, $MA_{0.5}FA_{0.5}PbI_3$, $MA_{0.65}FA_{0.3}EA_{0.05}PbI_3$, $MA_{0.53}FA_{0.38}EA_{0.09}PbI_3$, and $MA_{0.65}FA_{0.30}BA_{0.05}PbI_3$ perovskites, respectively. The remnant magnetization (M_r) is in the range of 0.16 to 0.27 emu g^{-1}, which indicates a soft ferromagnetic behavior. As a matter of fact, the alloy perovskites are far away from the related values of superparamagnetics with no hysteresis. However, the crystal orientation, the anisotropy, and the crystal size distribution have the potential to change the $M - H$ hysteresis curve.

To investigate the optoelectronic properties of these alloy perovskites, we measured the effective charge-carrier mobility in thin films using the optical pump-THz probe spectroscopy. The wavelength of the pump beam is 400 nm with an intensity of 40 μJ cm^{-2}. The THz time domain signals were collected in
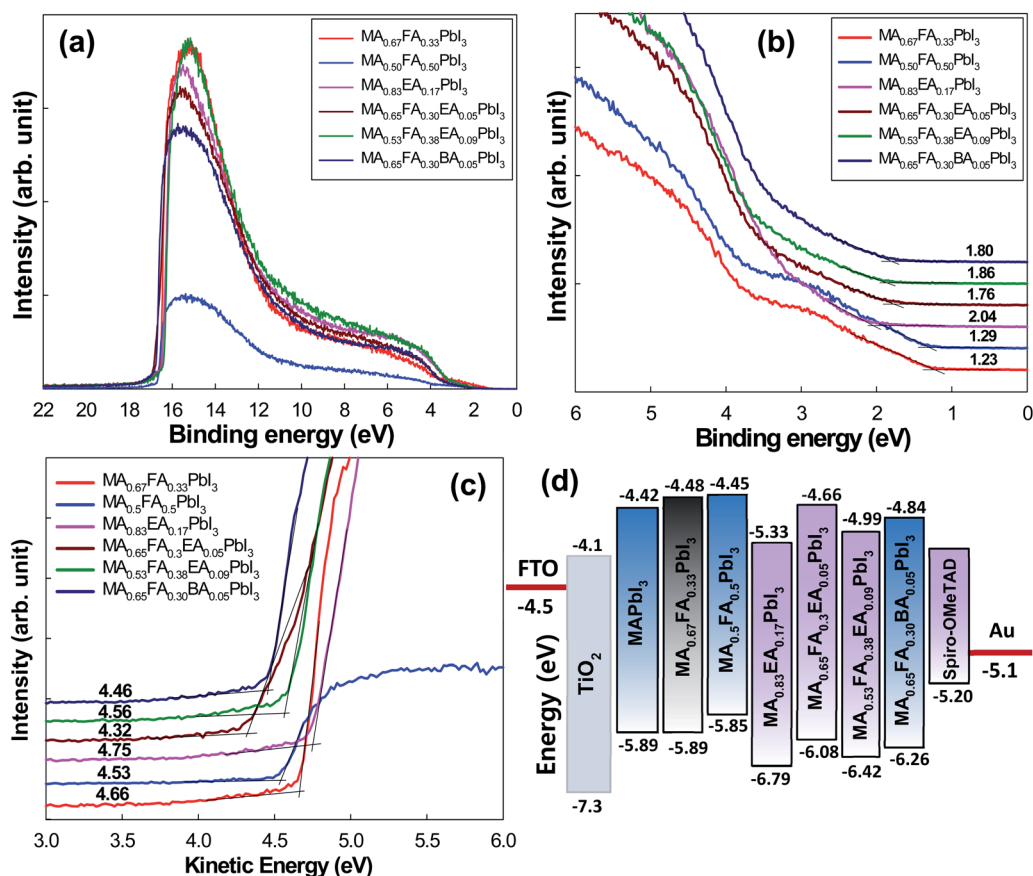

Fig. 9 The micro X-ray/UV photoelectron spectrometer characterization for the alloy perovskites/FTO substrate. (a) The wide binding energy range valence spectra, (b) the narrow binding energy range valence spectra, (c) the secondary-electron cutoffs for the work function determination, and the (d) energy level of the 3D $MAPbI_3$ and the alloy perovskites for the FTO/TiO$_2$/perovskite/Spiro-MeOTAD/Au solar cell configuration.
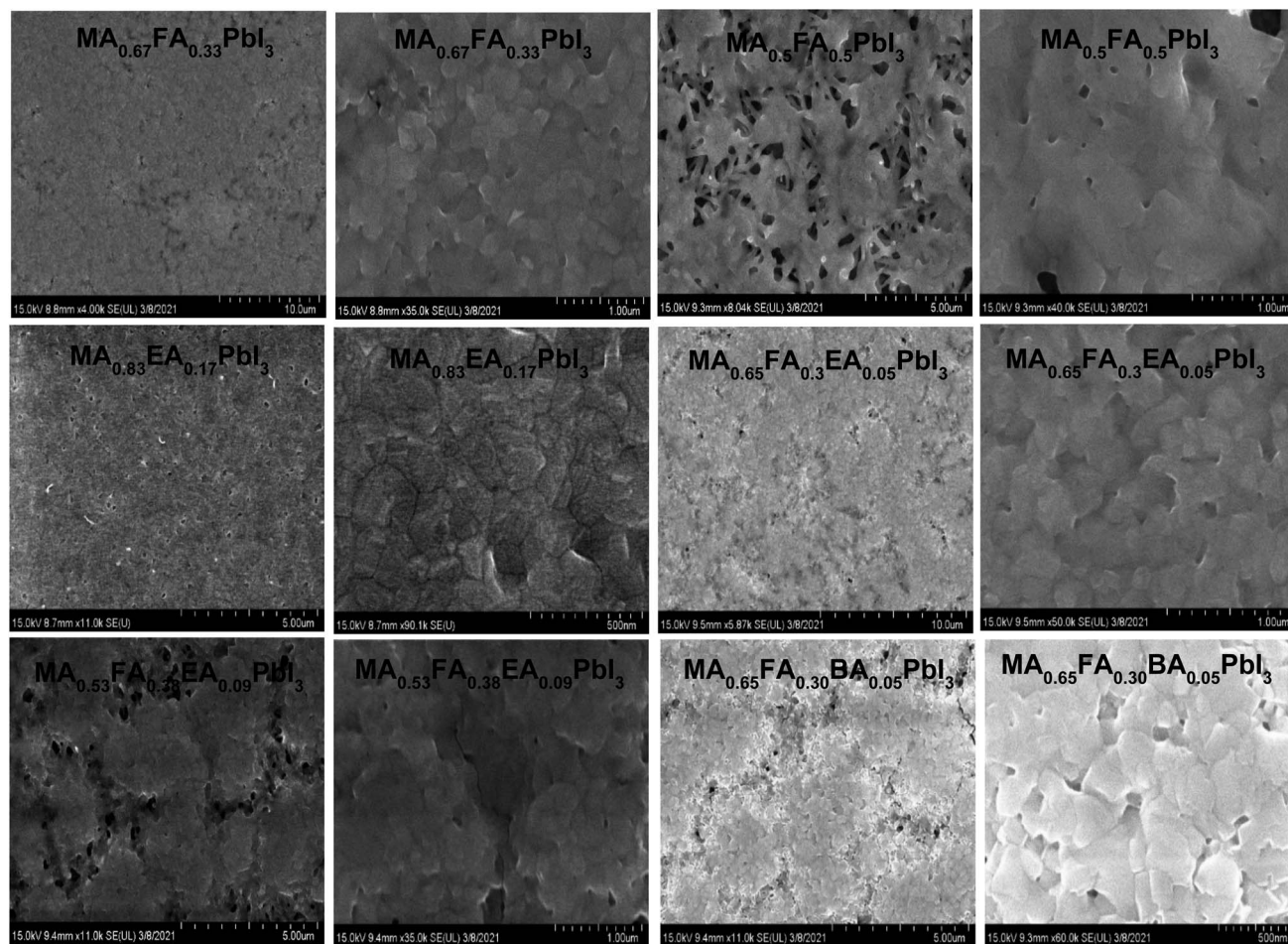
Fig. 10 Low and high resolution scanning electron microscopy (SEM) images of $MA_{0.67}FA_{0.33}PbI_3$, $MA_{0.5}FA_{0.5}PbI_3$, $MA_{0.83}EA_{0.17}PbI_3$, $MA_{0.65}FA_{0.3}EA_{0.05}PbI_3$, $MA_{0.53}FA_{0.38}EA_{0.09}PbI_3$, and $MA_{0.65}FA_{0.30}BA_{0.05}PbI_3$ perovskite films.

Table 2 The champion photovoltaic parameters of solar cells using 3D MAPbI$_3$ and alloy perovskites based on FTO/compact TiO$_2$/mesoporous TiO$_2$/perovskite/Spiro-MeOTAD/Au

Perovskites	J_{sc} [mA cm^{-2}]	V_{oc} [V]	FF [%]	η [%]
MAPbI$_3$	17.01	1.00	58.23	9.89
MA$_{0.67}$FA$_{0.33}$PbI$_3$	16.98	0.84	65.71	9.34
MA$_{0.5}$FA$_{0.5}$PbI$_3$	18.76	0.94	47.13	8.27
MA$_{0.83}$EA$_{0.17}$PbI$_3$	16.28	0.99	63.45	10.22
MA$_{0.65}$FA$_{0.3}$EA$_{0.05}$PbI$_3$	14.00	0.84	63.01	7.38
MA$_{0.53}$FA$_{0.38}$EA$_{0.09}$PbI$_3$	11.96	0.87	48.97	5.07
MA$_{0.65}$FA$_{0.30}$BA$_{0.05}$PbI$_3$	12.93	0.87	64.62	7.29

the spectral range from 0.2 to 2.5 THz. Upon photoexcitation, the fractional change in THz amplitude ($\Delta T/T$) was measured as a function of the time delay between the optical pump pulse and THz probe pulse. The $\Delta T/T$ signal can be changed into the photoinduced conductivity, which corresponds to the product of the carrier density and the mobility, μ.[34] Since these experiments do not contain the fraction φ of adsorbed photons that is changed into free charge-carrier pairs, the effective mobility,

$\varphi\mu$, can be calculated. Generally, because the excitonic effect of 3D perovskite can be negligible at room temperature, $\varphi = 1$, the effective charge mobility is regarded as the actual mobility. As shown in Fig. 8b, compared to 3D MAPbI$_3$ perovskite, the mobilities of all alloy perovskites were enhanced. This suggests that cubic structures of alloy perovskites have improved the orientation and are perpendicular to the substrate and thus show higher mobility than 3D perovskite. To assess the effectiveness of carrier transport, we measured the mobility of alloy perovskites using the hall effect measurement. The calculated carrier mobility is 8.02, 17.52, 14.71, 25.87, 19.02, 15.60 and 14.87 cm^2 V^{-1} s^{-1} for MAPbI$_3$, MA$_{0.67}$FA$_{0.33}$PbI$_3$, MA$_{0.5}$FA$_{0.5}$PbI$_3$, MA$_{0.83}$EA$_{0.17}$PbI$_3$, MA$_{0.65}$FA$_{0.3}$EA$_{0.05}$PbI$_3$, MA$_{0.53}$FA$_{0.38}$EA$_{0.09}$PbI$_3$, and MA$_{0.65}$FA$_{0.30}$BA$_{0.05}$PbI$_3$ perovskites, respectively. The mobility of the 3D MAPbI$_3$ perovskite is similar to that of the previous 3D MAPbI$_3$ thin films, which exhibit the charge-carrier mobility in the range of from 1 to 11.6 cm^2 V^{-1} s^{-1} (ref. 33) and it was improved to 36.0 cm^2 V^{-1} s^{-1} by the thermal annealing process.[34] Compared to 3D MAPbI$_3$ perovskite film, the alloy perovskite films display increased mobility due to the higher charge carrier concentration and conductivity, as mentioned in Fig. 8b. That is, the defect density in alloy perovskite films was
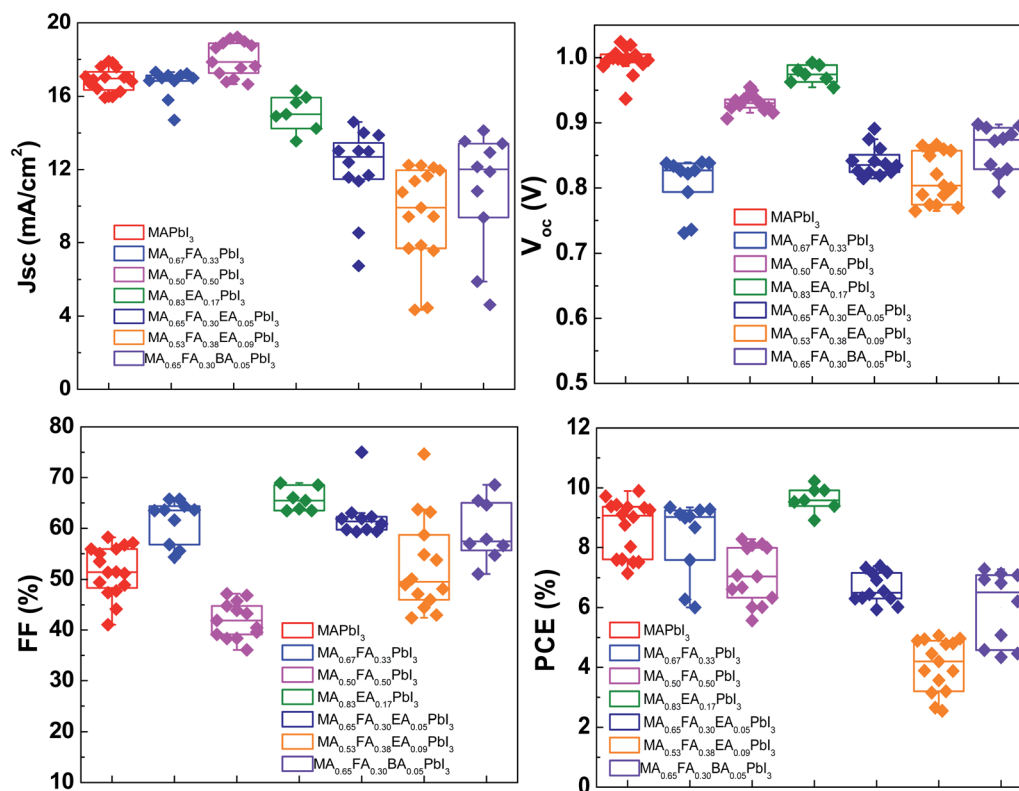
Fig. 11 The photovoltaic performance, which is the $J-V$ curve obtained from a forward scan, of the alloy perovskite solar cells made with regular structure (FTO/TiO$_2$ BL/TiO$_2$ MP/alloy perovskites/Spiro-OMeTAD) under simulated AM (air mass) 1.5 G (global) illumination (100 mW cm^{-2}).

reduced compared to control film, MAPbI$_3$, resulting in the enhancement in photo-carrier transport.

The adequate energy band structure of the perovskites between the conduction band minimum (CBM) and the valence band minimum (VBM) is important to make the charge extraction efficient from the perovskites and to facilitate the electron/hole transport in the photovoltaic application. The electronic structure of 2D perovskites was studied by UPS, which is illustrated in Fig. 9. For each compound, the top panel shows the UPS survey spectra and the homo level states, which are shown in Fig. 9a and b. The bottom panel shows the photoemission cut-off, from which the work function of the surface is extracted, and it is displayed in Fig. 9c. Even though the VBM is determined from the first ionization energy at low binding energy, the position of the CBM relative to the vacuum level (E_{vac}) was estimated from the difference between the optical band gap and the VBM position.[35,36] All the energies are referenced to a common Fermi level (E_{F}) of the Au substrate (0 eV). Fig. 9d shows the alignment of the energy level of the alloy perovskite series when it was applied into an FTO/TiO$_2$/perovskite/Spiro-MeOTAD/Au solar cell configuration. The 3D MA$_{1-x}$FA$_x$PbI$_3$ perovskites exhibited the VBM energy closer to the highest occupied molecular orbital (HOMO) level of the HTL, which indicated that there was no hole extraction barrier. However, the EA cation and the BA cation incorporated into the MA$_{1-x}$FA$_x$PbI$_3$ perovskites showed a larger barrier compared to MA$_{1-x}$FA$_x$PbI$_3$ perovskites. The lowest unoccupied molecular

orbital (LUMO) level of the HTL is positioned above the CBM of perovskites, which indicates a large barrier to prevent electron loss at the interface between the perovskites and the HTL layer. Since the HOMO level of the HTL was in a position 100 meV lower than the perovskite VBM, the built-in field and the collection of the hole were constrained, which caused the V_{oc} to decrease from the device point of view. As shown in Fig. 9d, the deeper CBM of MA$_{0.83}$EA$_{0.17}$PbI$_3$ perovskite film can reduce the recombination possibility of electrons from the perovskite with the hole in the HTL layer, which is beneficial to the enhancement of V_{oc}, whereas the gap between the VBM of MA$_{0.83}$-EA$_{0.17}$PbI$_3$ and the HOMO level of HTL is large compared to the other film, which would become the barrier of hole extraction at the perovskite/HTL interface. However, the film morphology of the MA$_{0.83}$EA$_{0.17}$PbI$_3$ perovskite film shows the most packed and uniform film among perovskites (Fig. 10). Thus, the highest efficiency in MA$_{0.83}$EA$_{0.17}$PbI$_3$ based device was achieved compared to the other perovskite devices (Table 2). This indicates that both the intrinsic and physical properties of the films affect the device performance.

The morphology of the perovskite alloy films is shown in Fig. 10. The SEM image of MAPbI$_3$ (Fig. S2†) shows dendritic crystalline aggregates in several places. However, the MA$_{0.67}$-FA$_{0.33}$PbI$_3$, MA$_{0.83}$EA$_{0.17}$PbI$_3$, and MA$_{0.65}$FA$_{0.3}$EA$_{0.05}$PbI$_3$ perovskite films display a compact polycrystalline grain texture and a pinhole-free morphology that fully cover the MP-TiO$_2$ substrate. With the MA$_{0.53}$FA$_{0.38}$EA$_{0.09}$PbI$_3$ and
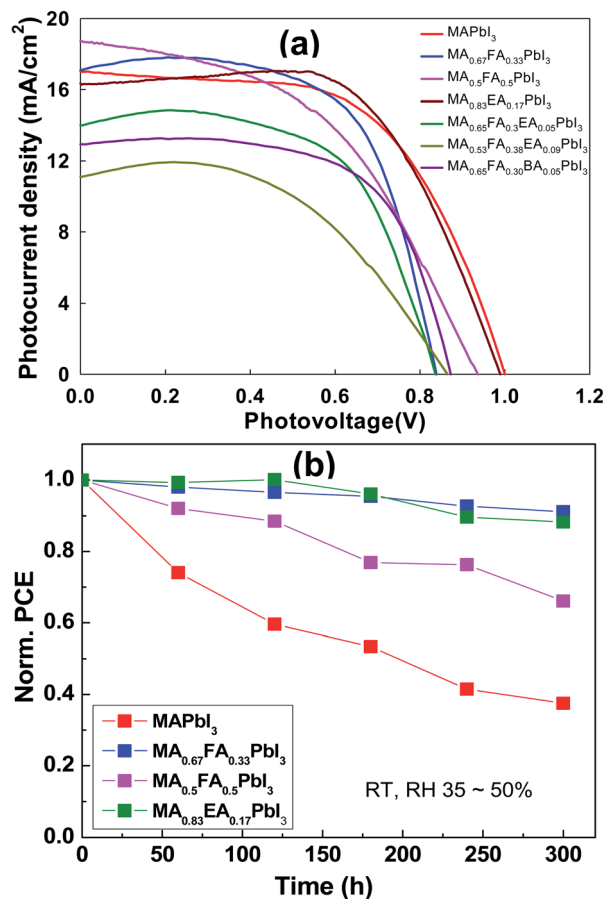
Fig. 12 (a) The photovoltaic performance, which is the $J-V$ curve obtained from the alloy perovskite solar cells made with regular structure (FTO/TiO$_2$ BL/TiO$_2$ MP/alloy perovskites/Spiro-OMeTAD) under simulated AM (air mass) 1.5 G (global) illumination (100 mW cm^{-2}). (b) The stability test of unencapsulated MAPbI$_3$ and alloy perovskites devices at room temperature and a relative humidity condition of 35–50%.

MA$_{0.65}$FA$_{0.30}$BA$_{0.05}$PbI$_3$ perovskite films, it was observed that there were some pinholes in the films, which is more severe in the MA$_{0.5}$FA$_{0.5}$PbI$_3$ perovskite film. This result is well consistent with the lowest fill factor in MA$_{0.5}$FA$_{0.5}$PbI$_3$ perovskite based devices, as shown in Fig. 12. In addition, this suggests that the precursor solution of these perovskites should make a highly supersaturated concentration, which exists with a large number of uniformly distributed nuclei in the precursor solution.[37]

The planar devices were fabricated with n–i–p PSCs with a configuration of FTO/blocking TiO$_2$/*meso*-TiO$_2$/3D or an alloy perovskite layer/Spiro-OMeTAD/Au. The PSC distributions of MAPbI$_3$ and alloy perovskite based devices are displayed in Fig. 11. The MAPbI$_3$ cells achieved an average PCE 8.67 ± 0.93% with a V_{oc} of 1.00 ± 0.02 V, J_{sc} of 16.87 ± 0.65 mA cm^{-2}, and an FF of 51.56 ± 4.94%. The MA$_{0.67}$FA$_{0.33}$PbI$_3$ and MA$_{0.5}$FA$_{0.5}$PbI$_3$ cells show a comparable J_{sc}, 16.69 ± 0.82 mA cm^{-2} and 18.02 ± 0.96 mA cm^{-2}, respectively, to the MAPbI$_3$ cells, however these devices have a much lower average V_{oc} of 0.81 ± 0.04 V for MA$_{0.67}$FA$_{0.33}$PbI$_3$ and FF of 41.96 ± 3.59% for MA$_{0.5}$FA$_{0.5}$PbI$_3$ to the MAPbI$_3$ cells, resulting in average PCE 8.36 ± 1.28% and

7.06 ± 0.94%, respectively. The J_{sc} (15.08 ± 0.97 mA cm^{-2}) and V_{oc} (0.97 ± 0.01%) of MA$_{0.83}$EA$_{0.17}$PbI$_3$ devices is lower than that of MAPbI$_3$ cells. But, it exhibits significantly improved FF, 65.67 ± 2.32%, compared to MAPbI$_3$, resulting in an improved PCE of 9.64 ± 0.43%. The MA$_{0.65}$FA$_{0.3}$EA$_{0.05}$PbI$_3$, MA$_{0.53}$FA$_{0.38}$EA$_{0.09}$-PbI$_3$, and MA$_{0.65}$FA$_{0.30}$BA$_{0.05}$PbI$_3$ cells show improved FF, 62.32 ± 4.65%, 52.78 ± 9.37%, and 59.47 ± 6.04%, respectively, compared to MAPbI$_3$. However, J_{sc} and V_{oc} of these cells show less than that of MAPbI$_3$, yielding PCE of 6.65 ± 0.51%, 4.06 ± 0.87%, and 5.99 ± 1.23%, respectively. The $J_{sc}-V_{oc}$ curves of the champion cells are presented in Fig. 12a, and the photovoltaic parameters are summarized in Table 2. The MA$_{0.83}$EA$_{0.17}$PbI$_3$ perovskite cell presented a champion PCE of 10.22% along with J_{sc} of 16.28 mA cm^{-2}, V_{oc} of 0.99 V and FF of 63.45%, which is ascribed to the formation of higher quality perovskites with a low defect density favorable to the carrier transport. Long-term stability of alloy perovskite devices was investigated under ambient conditions (35–50% RH and 25 ± 3 °C). As shown in Fig. 12b, significant degradation of performances was observed in the 3D MAPbI$_3$ device over 300 h with 62.48% of its initial PCE (from 9.89% to 3.71%). Whereas MA$_{0.67}$FA$_{0.33}$PbI$_3$, MA$_{0.5}$FA$_{0.5}$PbI$_3$, and MA$_{0.83}$EA$_{0.17}$PbI$_3$ perovskites retains 91.12%, 66.08%, and 88.24% of their original PCE after 300 h. This result indicates that the migration of ions in alloy perovskites is inhibited to prevent degradation of the perovskite, thereby increasing the stability of the perovskite cell due to the increase in coulombic interactions between space cations existing in the 3D structure.

4. Conclusions

We have presented the alloy 3D perovskites with the incorporation of EA and BA cations into the 3D MA$_{1-x}$FA$_x$PbI$_3$ perovskites within the range that did not form the 2D perovskite phase. The incorporation of the cation plays an important role in the cubic phase stabilization because if it has a stronger dipole and more flexible orientation, it will result in a high degree of cation disorder. The alloy perovskites showed much more efficient exciton recombination, which decreased the generation of a free carrier compared to other perovskites. As a consequence, all of these situations have shown that the PL lifetimes of the alloyed perovskites do not improve significantly compared to the 3D perovskite, which is the MAPbI$_3$. All the alloy perovskites are far away from the related values of the superparamagnetics with no hysteresis. However, crystal orientation, anisotropy, and the crystal size distribution have the potential to change the M − H hysteresis curve. In the regular solar cell, n–i–p, the PCE of the MA$_{0.83}$EA$_{0.17}$PbI$_3$ perovskite solar cell shows the highest efficiency of 10.22% under 1 sun illumination.

Conflicts of interest

There are no conflicts to declare.

Acknowledgements

References

1 T. M. Koh, K. Fu, Y. Fang, S. Chen, T. C. Sum, N. Mathews, S. G. Mhaisalkar, P. P. Boix and T. Baikie, *J. Phys. Chem. C*, 2014, **118**, 16458–16462.

2 Q. Han, S.-H. Bae, P. Sun, Y.-T. Hsieh, Y. Yang, Y. S. Rim, H. Zhao, Q. Chen, W. Shi, G. Li and Y. Yang, *Adv. Mater.*, 2016, **28**, 2253–2258.

3 M. T. Weller, O. J. Weber, J. M. Frost and A. Walsh, *J. Phys. Chem. Lett.*, 2015, **6**, 3209–3212.

4 F. Ma, J. Li, W. Li, N. Lin, L. Wang and J. Qiao, *Chem. Sci.*, 2017, **8**, 800–805.

5 N. J. Jeon, J. H. Noh, W. S. Yang, Y. C. Kim, S. Ryu, J. Seo and S. I. Seok, *Nature*, 2015, **517**, 476.

6 D. P. McMeekin, G. Sadoughi, W. Rehman, G. E. Eperon, M. Saliba, M. T. Hörantner, A. Haghighirad, N. Sakai, L. Korte, B. Rech, M. B. Johnston, L. M. Herz and H. J. Snaith, *Science*, 2016, **351**, 151–155.

7 K. Yan, M. Long, T. Zhang, Z. Wei, H. Chen, S. Yang and J. Xu, *J. Am. Chem. Soc.*, 2015, **137**, 4460–4468.

8 L. N. Quan, M. Yuan, R. Comin, O. Voznyy, E. M. Beauregard, S. Hoogland, A. Buin, A. R. Kirmani, K. Zhao, A. Amassian, D. H. Kim and E. H. Sargent, *J. Am. Chem. Soc.*, 2016, **138**, 2649–2655.

9 H. Tsai, W. Nie, J.-C. Blancon, C. C. Stoumpos, R. Asadpour, B. Harutyunyan, A. J. Neukirch, R. Verduzco, J. J. Crochet, S. Tretiak, L. Pedesseau, J. Even, M. A. Alam, G. Gupta, J. Lou, P. M. Ajayan, M. J. Bedzyk, M. G. Kanatzidis and A. D. Mohite, *Nature*, 2016, **536**, 312.

10 R. Yang, R. Li, Y. Cao, Y. Wei, Y. Miao, W. L. Tan, X. Jiao, H. Chen, L. Zhang, Q. Chen, H. Zhang, W. Zou, Y. Wang, M. Yang, C. Yi, N. Wang, F. Gao, C. R. McNeill, T. Qin, J. Wang and W. Huang, *Adv. Mater.*, 2018, **30**, 1804771.

11 M. I. Saidaminov, A. L. Abdelhady, B. Murali, E. Alarousu, V. M. Burlakov, W. Peng, I. Dursun, L. Wang, Y. He, G. Maculan, A. Goriely, T. Wu, O. F. Mohammed and O. M. Bakr, *Nat. Commun.*, 2015, **6**, 7586.

12 L. Chen, Y.-Y. Tan, Z.-X. Chen, T. Wang, S. Hu, Z.-A. Nan, L.-Q. Xie, Y. Hui, J.-X. Huang, C. Zhan, S.-H. Wang, J.-Z. Zhou, J.-W. Yan, B.-W. Mao and Z.-Q. Tian, *J. Am. Chem. Soc.*, 2019, **141**, 1665–1671.

13 L.-Q. Xie, L. Chen, Z.-A. Nan, H.-X. Lin, T. Wang, D.-P. Zhan, J.-W. Yan, B.-W. Mao and Z.-Q. Tian, *J. Am. Chem. Soc.*, 2017, **139**, 3320–3323.

14 W.-G. Li, H.-S. Rao, B.-X. Chen, X.-D. Wang and D.-B. Kuang, *J. Mater. Chem. A*, 2017, **5**, 19431–19438.

15 J. W. Shin, K. Eom and D. Moon, *J. Synchrotron Radiat.*, 2016, **23**, 369–373.

16 Z. Otwinowski and W. Minor, in *Methods in Enzymology*, Academic Press, New York, 1997, vol. 276.

17 G. M. Sheldrick, *Acta Crystallogr., Sect. A: Found. Crystallogr.*, 2015, **71**, 3–8.

18 G. M. Sheldrick, *Acta Crystallogr., Sect. C: Cryst. Struct. Commun.*, 2015, **71**, 3–8.

19 K. Chondroudis, T. J. McCarthy and M. G. Kanatzidis, *Inorg. Chem.*, 1996, **35**, 840–844.

20 T. J. McCarthy and M. G. Kanatzidis, *Inorg. Chem.*, 1995, **34**, 1257–1267.

21 J. Park, C. Kim, J. Lee, C. Yim, C. H. Kim, J. Lee, S. Jung, J. Ryu, H.-S. Kang and T. Joo, *Rev. Sci. Instrum.*, 2011, **82**, 013305.

22 H.-S. Kim, J.-W. Lee, N. Yantara, P. P. Boix, S. A. Kulkarni, S. Mhaisalkar, M. Grätzel and N.-G. Park, *Nano Lett.*, 2013, **13**, 2412–2417.

23 O. J. Weber, B. Charles and M. T. Weller, *J. Mater. Chem. A*, 2016, **4**, 15375–15382.

24 G. Kieslich, S. Sun and A. K. Cheetham, *Chem. Sci.*, 2014, **5**, 4712–4715.

25 W. Travis, E. N. K. Glover, H. Bronstein, D. O. Scanlon and R. G. Palgrave, *Chem. Sci.*, 2016, **7**, 4548–4556.

26 X. Lian, J. Chen, M. Qin, Y. Zhang, S. Tian, X. Lu, G. Wu and H. Chen, *Angew. Chem., Int. Ed.*, 2019, **58**, 9409–9413.

27 G. Lv, L. Li, D. Lu, Z. Xu, Y. Dong, Q. Li, Z. Chang, W.-J. Yin and Y. Liu, *Nano Lett.*, 2021, **21**, 5788–5797.

28 E. P. Booker, T. H. Thomas, C. Quarti, M. R. Stanton, C. D. Dashwood, A. J. Gillett, J. M. Richter, A. J. Pearson, N. J. L. K. Davis, H. Sirringhaus, M. B. Price, N. C. Greenham, D. Beljonne, S. E. Dutton and F. Deschler, *J. Am. Chem. Soc.*, 2017, **139**, 18632–18639.

29 C. Quarti, N. Marchal and D. Beljonne, *J. Phys. Chem. Lett.*, 2018, **9**, 3416–3424.

30 L. Mao, H. Tsai, W. Nie, L. Ma, J. Im, C. C. Stoumpos, C. D. Malliakas, F. Hao, M. R. Wasielewski, A. D. Mohite and M. G. Kanatzidis, *Chem. Mater.*, 2016, **28**, 7781–7792.

31 X. Wu, M. T. Trinh, D. Niesner, H. Zhu, Z. Norman, J. S. Owen, O. Yaffe, B. J. Kudisch and X. Y. Zhu, *J. Am. Chem. Soc.*, 2015, **137**, 2089–2096.

32 M. U. Rothmann, W. Li, Y. Zhu, U. Bach, L. Spiccia, J. Etheridge and Y.-B. Cheng, *Nat. Commun.*, 2017, **8**, 14547.

33 C. Wehrenfennig, G. E. Eperon, M. B. Johnston, H. J. Snaith and L. M. Herz, *Adv. Mater.*, 2014, **26**, 1584–1589.

34 R. L. Milot, R. J. Sutton, G. E. Eperon, A. A. Haghighirad, J. Martinez Hardigree, L. Miranda, H. J. Snaith, M. B. Johnston and L. M. Herz, *Nano Lett.*, 2016, **16**, 7001–7007.

35 A. Kahn, *Mater. Horiz.*, 2016, **3**, 7–10.

36 P. Schulz, E. Edri, S. Kirmayer, G. Hodes, D. Cahen and A. Kahn, *Energy Environ. Sci.*, 2014, **7**, 1377–1381.

37 F. Huang, Y. Dkhissi, W. Huang, M. Xiao, I. Benesperi, S. Rubanov, Y. Zhu, X. Lin, L. Jiang, Y. Zhou, A. Gray-Weale, J. Etheridge, C. R. McNeill, R. A. Caruso, U. Bach, L. Spiccia and Y.-B. Cheng, *Nano Energy*, 2014, **10**, 10–18.